Inorganic Chemistry
Article
pubs.acs.org/IC

Unprecedented Conformational Variability in Main Group Inorganic Chemistry: the Tetraazidoarsenite and -Antimonite Salts $A^+[M(N_3)_4]^-$ ($A = NMe_4$, PPh_4, $(Ph_3P)_2N$; $M = As$, Sb), Five Similar Salts, Five Different Anion Structures

Ralf Haiges,* Martin Rahm, and Karl O. Christe*

Loker Hydrocarbon Research Institute and Department of Chemistry, University of Southern California, Los Angeles, California 90089, United States

Supporting Information

ABSTRACT: A unique example for conformational variability in inorganic main group chemistry has been discovered. The arrangement of the azido ligands in the pseudotrigonal bipyramidal $[As(N_3)_4]^-$ and $[Sb(N_3)_4]^-$ anions theoretically can give rise to seven different conformers which have identical MN_4 skeletons but different azido ligand arrangements and very similar energies. We have now synthesized and structurally characterized five of these conformers by subtle variations in the nature of the counterion. Whereas conformational variability is common in organic chemistry, it is rare in inorganic main group chemistry and is usually limited to two. To our best knowledge, the experimental observation of five distinct single conformers for the same type of anion is unprecedented. Theoretical calculations at the M06-2X/cc-pwCVTZ-PP level for all seven possible basic conformers show that (1) the energy differences between the five experimentally observed conformers are about 1 kcal/mol or less, and (2) the free monomeric anions are the energetically favored species in the gas phase and also for $[As(N_3)_4]^-$ in the solid state, whereas for $[Sb(N_3)_4]^-$ associated anions are energetically favored in the solid state and possibly in solutions. Raman spectroscopy shows that in the azide antisymmetric stretching region, the solid-state spectra are distinct for the different conformers, and permits their identification. The spectra of solutions are solvent dependent and differ from those of the solids indicating the presence of rapidly exchanging equilibria of different conformers. The only compound for which a solid with a single well-ordered conformer could not be isolated was $[N(CH_3)_4][As(N_3)_4]$ which formed a viscous, room-temperature ionic liquid. Its Raman spectrum was identical to that of its CH_3CN solution indicating the presence of an equilibrium of multiple conformers.

■ INTRODUCTION

Conformational variability in inorganic main group chemistry is rare and the number of observable conformers is usually limited to two.[1] In the course of our systematic study of group 15 tetraazidoanions, we have surprisingly discovered five(!) different conformers for these anions which all have the same MN_4 skeletons but differ in the arrangements of their azido ligands. During the past two years, we have carried out an experimental and theoretical study of the different conformers which are summarized in this paper.

Polyazido compounds are of general interest for energetic materials and have been the focus of numerous experimental studies in recent years.[2] Thus, the following binary group 15 polyazides have previously been synthesized: $P(N_3)_3$,[3a] $P(N_3)_5$,[3a] $[P(N_3)_6]^-$,[3b,c] $As(N_3)_3$,[3d,e,4] $[As(N_3)_4]^-$,[5] $As(N_3)_5$,[6] $[As(N_3)_4]^+$,[5] $[As(N_3)_6]^-$,[3f,5] $Sb(N_3)_3$,[3g,4] $[Sb(N_3)_4]^-$,[5] $[Sb(N_3)_5]^{2-}$,[7] $Sb(N_3)_5$,[6] $[Sb(N_3)_4]^+$,[5] and $[Sb(N_3)_6]^-$,[5,6] $Bi(N_3)_3$,[2,8,9] $[Bi(N_3)_4]^-$,[2,8] $[Bi(N_3)_5]^{2-}$,[2] and $[Bi(N_3)_6]^{3-}$[2,8] although only $[P(N_3)_6]^-$,[3c] $As(N_3)_3$,[4] $[As(N_3)_6]^-$,[3f,5] $Sb(N_3)_3$,[4] $[Sb(N_3)_5]^{2-}$,[7] $[Sb(N_3)_6]^-$,[6,7] $[Bi(N_3)_4]^-$,[2,8] $[Bi(N_3)_5]^{2-}$,[2] and $[Bi(N_3)_6]^{3-}$[2,8] have been structurally characterized. Very recently, the synthesis and structural characterization of $[PPh_4][As(N_3)_4]$ and $[PPh_4][Sb(N_3)_4]$ have also been reported.[10]

■ EXPERIMENTAL SECTION

Caution! *While the compounds described in this manuscript are quite stable and no explosion occurred during the course of this study, many polyazides are extremely shock-sensitive and can explode violently upon the slightest provocation. As a result, these materials should be handled only on a very small scale using appropriate safety precautions.*[11] ***Ignoring safety precautions may lead to serious injuries!***

Materials and Apparatus. All reactions were carried out in Teflon-FEP ampules that were closed by stainless steel valves. Volatile materials were handled in a Pyrex glass vacuum line. Nonvolatile materials were handled in the dry nitrogen atmosphere of a glovebox. Raman spectra were recorded in the Teflon-FEP reactors or in heat-sealed Pyrex glass melting point capillaries in the range of 4000−80 cm^{-1} on a Bruker Equinox 55 FT-RA spectrophotometer using a Nd:YAG laser at 1064 nm with *power levels less than 100 mW*. Infrared spectra were recorded in

Received: October 9, 2012
Published: December 7, 2012

the range 4000−400 cm^{-1} on a Midac, M Series, FT-IR spectrometer using KBr pellets. The pellets were prepared inside the glovebox using an Econo mini-press (Barnes Engineering Co.). NMR spectra were recorded at 298 K on Bruker AMX 500 (^{14}N, ν_0 = 36.13 MHz) and Varian VNMRS-600s (^{15}N, ν_0 = 60.79 MHz) spectrometers using $(CD_3)_2CO$ and CD_3CN solutions in 5 mm glass tubes that were sealed with a J. Young valve. Neat CH_3NO_2 (δ = 0.00 ppm) was used as external reference. Differential Thermal Analysis (DTA) curves were recorded with a purge of dry nitrogen gas on an OZM Research DTA552-Ex instrument using the Meavy 2.2.0 software. The heating rate was 5 °C/min, and the sample size 20−30 mg. SbF_3 (Ozark Mahoning) was used without further purification. AsF_3 (Advanced Research Chemicals) and Me_3SiN_3 (Aldrich) were purified by fractional condensation prior to use. Solvents were dried by standard methods and freshly distilled prior to use. NMe_4N_3, PPh_4N_3, and $(Ph_3P)_2NN_3$ ($(Ph_3P)_2N$ = bis(triphenylphosphoranylidene)ammonium) were prepared by ion-exchange from NMe_4Cl, PPh_4Cl and $(Ph_3P)_2NCl$, respectively.[12]

Preparation of A[As(N$_3$)$_4$] (A = NMe$_4$, PPh$_4$, (Ph$_3$P)$_2$N). A sample of AN_3 (1.00 mmol) was loaded into a Teflon-FEP ampule, followed by the addition of 4 mL acetonitrile in vacuo at −196 °C. The mixture was warmed to ambient temperature to form a clear solution. After cooling to −196 °C, AsF_3 (1.00 mmol) and Me_3SiN_3 (4.0 mmol) were condensed into the vessel. The mixture was then allowed to warm to ambient temperature over a period of about 30 min. After 10 h at room temperature, a clear, colorless solution was obtained. The temperature was lowered to −20 °C, and all volatile material was pumped off. After additional pumping for 24 h at ambient temperature a clear colorless liquid (A = NMe_4) or crystalline colorless solids (A = PPh_4, $(Ph_3P)_2N$) were obtained. Weights expected for 1.00 mmol of $[NMe_4][As(N_3)_4]$, $[PPh_4][As(N_3)_4]$, and $[(Ph_3P)_2N][As(N_3)_4]$: 0.317 g, 0.582 g, and 0.782 g; weights found: 0.328 g, 0.575 g, and 0.789 g, respectively.

[NMe$_4$][As(N$_3$)$_4$]. DTA decomposition onset: 75 °C (explosion); ^{14}N NMR (CD_3CN, 298 K): $\delta = -137.4$ ppm (shoulder next to CH_3CN) (N_β), −243 ppm ($\tau_{1/2}$ = 240 Hz) (N_γ), −337.2 ppm ($\tau_{1/2}$ = 4 Hz) (NMe_4); Raman (50 mW, −40 °C): 3035 (3.6), 2982 (5.5), 2956 (2.7), 2924 (3.6), 2896 (0.9), 2872 (0.1), 2819 (0.9), 2130 (5.5), 2093 (2.7), 2014 (0.9), 1451 (1.8), 1332 (2.7), 1270 (0.9), 951 (0.9), 754 (1.8), 672 (2.7), 573 (0.1), 550 (0.0+), 538 (0.0+), 465 (10.0), 420 (2.7), 293 (1.8), 247 (1.8) cm^{-1}; IR (KBr): 3014 (m), 2085 (m), 2035 (vs), 2023 (vs), 2011 (s), 1487 (s), 1408 (w), 1400 (w), 1257 (vw), 956 (m), 948 (m), 845 (vw), 802 (mw), 418 (s) cm^{-1}.

[PPh$_4$][As(N$_3$)$_4$]. DTA decomposition onset: 87 °C (explosion); ^{14}N NMR ($(CD_3)_2CO$, 298 K): $\delta = -136.9$ ppm ($\tau_{1/2}$ = 19 Hz) (N_β), −246 ppm ($\tau_{1/2}$ = 180 Hz) (N_γ); ^{14}N NMR (CD_3CN, 298 K): $\delta = -137.6$ ppm (shoulder next to CH_3CN) (N_β), −243 ppm ($\tau_{1/2}$ = 320 Hz) (N_γ); Raman (40 mW, 20 °C): 3170 (0.4), 3145 (0.9), 3090 (2.2), 3066 (10.0), 3010 (0.4), 3010 (0.4), 2116 (2.6), 2089 (0.9), 2060 (0.1), 2049 (0.1), 2020 (0.9), 1587 (3.9), 1576 (0.9), 1484 (0.0), 1443 (0.4), 1437 (0.4), 1324 (0.9), 1276 (0.9), 1188 (0.9), 1167 (0.9), 1111 (0.9), 1101 (1.7), 1073 (0.0), 1027 (2.6), 1001 (7.4), 987 (0.4), 940 (0.4), 933 (0.0), 757 (0.0), 727 (0.4), 682 (2.2), 651 (0.4), 617 (0.9), 535 (0.0), 528 (0.0), 466 (3.9), 428 (0.9), 393 (0.4), 334 (0.9), 298 (0.9), 276 (1.7), 267 (1.3), 254 (2.6), 239 (1.3), 200 (2.6), 200 (2.6), 160 (5.7) cm^{-1}; IR (KBr): 3086 (w), 3061 (w), 2203 (vw), 2145 (w), 2112 (s), 2085 (vs), 2045 (vs), 2036 (vs), 2017 (vs), 1984 (s), 1973 (ms), 1584 (mw), 1574 (w), 1481 (m), 1440 (ms), 1437 (s), 1434 (ms), 1394 (w), 1359 (vw), 1341 (w), 1315 (mw), 1259 (m), 1250 (ms), 1185 (w), 1164 (w), 1160 (w), 1108 (s), 1023 (w), 994 (m), 853 (vw), 801 (w), 759 (ms), 754 (ms), 724 (s), 690 (s), 648 (w), 615 (w), 602 (vw), 571 (vw), 528 (vs), 464 (mw), 446 (w), 443 (w), 440 (w), 435 (mw), 424 (ms) cm^{-1}.

[(Ph$_3$P)$_2$N][As(N$_3$)$_4$]. DTA decomposition onset: 85 °C; ^{14}N NMR (CD_3CN, 298 K): $\delta = -137.2$ ppm (shoulder next to CH_3CN) (N_β), −241 ppm ($\tau_{1/2}$ = 200 Hz) (N_γ); Raman (75 mW, −40 °C): 3176 (0.4), 3148 (0.6), 3058 (10.0), 3014 (0.7), 2994 (0.6), 2961 (0.4), 2108 (1.9), 2085 (0.7), 2058 (1.9), 2023 (0.1), 1591 (4.7), 1577 (1.4), 1486 (0.1), 1442 (0.3), 1326 (0.7), 1282 (0.9), 1260 (0.3), 1187 (0.7), 1166 (0.9), 1113 (2.1), 1076 (0.1), 1030 (2.6), 1002 (7.3), 940 (0.3), 859 (0.1), 800 (0.1), 757 (0.1), 729 (0.4), 683 (0.1), 666 (2.0), 618 (1.0), 550 (0.1), 490 (0.3), 455 (3.4), 424 (0.7), 360 (0.7), 342 (1.1), 281 (0.1sh), 270 (2.0), 265 (0.1sh), 240 (2.9), 231 (0.1sh), 200 (1.7) cm^{-1}; IR (KBr) 3077 (vw), 3054 (w), 3022 (vw), 2992 (vw), 2105 (vs), 2082 (vs), 2056 (s), 2024 (vs), 1825 (vw), 1772 (vw), 1587 (mw), 1573 (w), 1482 (mw), 1436 (vs), 1315 (s), 1291 (s), 1270 (vs), 1246 (s), 1183 (m), 1158 (w), 1116 (vs), 1073 (w), 1025 (w), 997 (m), 932 (vw), 851 (vw), 796 (w), 757 (m), 748 (m), 724 (vs), 693 (vs), 616 (w), 547 (s), 533 (vs), 527 (s), 502 (s), 451 (mw), 449 (mw), 440 (w), 436 (w), 429 (w), 424 (m), 419 (m), 415 (m) cm^{-1}.

Preparation of A[Sb(N$_3$)$_4$] (A = NMe$_4$, PPh$_4$, (Ph$_3$P)$_2$N). Mixtures of AN_3 (1.00 mmol) and SbF_3 (1.00 mmol) were loaded into a Teflon-FEP ampule, followed by the addition of 4 mL of acetonitrile and Me_3SiN_3 (4.0 mmol) in vacuo at −196 °C. The resulting mixtures were then allowed to warm to ambient temperature over a period of about 30 min. After 10 h at room temperature, clear, colorless solutions were obtained. The temperature was lowered to −20 °C, and all volatile material was pumped off. After additional pumping for 24 h at ambient temperature crystalline colorless solids were obtained. Weights expected for 1.00 mmol of $[NMe_4][Sb(N_3)_4]$, $[PPh_4][Sb(N_3)_4]$, and $[(Ph_3P)_2N][Sb(N_3)_4]$: 0.364 g, 0.629 g, and 0.828 g; weights found: 0.355 g, 0.634 g, and 0.835 g, respectively.)

[NMe$_4$][Sb(N$_3$)$_4$]. DTA decomposition onset: 204 °C (explosion); ^{15}N NMR (CD_3CN, 298 K): $\delta = -137.8$ ppm ($\tau_{1/2}$ = 11 Hz) (N_β), −251.6 ppm ($\tau_{1/2}$ = 11 Hz) (N_γ), −337.2 ppm ($\tau_{1/2}$ = 1 Hz) (NMe_4); ^{14}N NMR (CD_3CN, 298 K): $\delta = -137.5$ ppm (shoulder next to CH_3CN) (N_β), −251 ppm ($\tau_{1/2}$ = 270 Hz) (N_γ), −337.1 ppm ($\tau_{1/2}$ = 4 Hz) (NMe_4); Raman (75 mW, −40 °C): 3035 (3.2), 2983 (2.7), 2958 (1.6), 2942 (1.1), 2926 (2.7), 2897 (0.5), 2819 (0.9), 2254 (0.5), 2100 (3.6), 2067 (2.5), 2040 (2.0), 2001 (0.2), 1995 (0.2), 1912 (0.2), 1485 (0.5), 1451 (2.0), 1420 (0.5), 1336 (3.0), 1336 (3.0), 1282 (1.8), 1221 (0.5), 1179 (0.5), 1078 (0.5), 957 (0.9), 932 (0.5), 921 (0.5), 760 (1.4), 760 (1.4), 654 (1.4), 614 (0.5), 606 (0.5), 462 (0.9), 401 (10.0), 379 (2.0), 307 (2.3), 288 (1.6), 236 (1.8), 227 (1.6), 227 (1.6), 180 (3.2), 180 (3.2), 102 (6.4) cm^{-1}, IR (KBr): 3017 (m), 2979 (w), 2035 (vs), 1645 (w), 1624 (w), 1488 (s), 1408 (m), 1321 (m), 1275 (w), 956 (s), 947 (s), 418 (m), 396 (w) cm^{-1}.

[PPh$_4$][Sb(N$_3$)$_4$]. DTA decomposition onset: 202 °C; ^{14}N NMR (CD_3CN, 298 K): $\delta = -137.6$ ppm (shoulder next to CH_3CN) (N_β), −253 ppm ($\tau_{1/2}$ = 220 Hz) (N_γ); Raman (60 mW, 20 °C): 3173 (0.5), 3147 (0.5), 3086 (2.5), 3063 (10.0), 3013 (1.0), 2960 (0.5), 2099 (3.0), 2072 (2.5), 2056 (1.0), 2037 (1.0), 2025 (1.0), 1589 (4.5), 1578 (1.5), 1485 (0.5), 1442 (1.0), 1329 (2.5), 1276 (1.0), 1192 (1.5), 1170 (1.0), 1102 (2.5), 1074 (0.5), 1029 (3.5), 1003 (9.5), 948 (0.5), 766 (0.5), 727 (1.0), 683 (2.0), 662 (1.0), 618 (2.0), 527 (0.5), 418 (9.5), 392 (2.5), 322 (2.5), 296 (1.5), 257 (3.0), 234 (2.0), 206 (3.0) cm^{-1}, IR (KBr): 3078 (vw), 3058 (vw), 2144 (w), 2099 (s), 2071 (vs), 2050 (s), 2036 (vs), 2023 (vs), 1635 (w), 1586 (w), 1483 (mw), 1443 (m), 1439 (m), 1319 (m), 1267 (m), 1187 (w), 1164 (w), 1107 (ms), 1025 (vw), 995 (mw), 856 (vw), 764 (m), 723 (ms), 690 (m), 640 (vw), 616 (w), 603 (vw), 590 (vw), 569 (vw), 548 (vw), 525 (s), 430 (mw) cm^{-1}.

[(Ph$_3$P)$_2$N][Sb(N$_3$)$_4$]. DTA decomposition onset: 210 °C; ^{14}N NMR (CD_3CN, 298 K): $\delta = -137.4$ ppm (shoulder next to CH_3CN) (N_β), −255 ppm ($\tau_{1/2}$ = 250 Hz) (N_γ); Raman (75 mW, −40 °C): 3177 (0.4), 3147 (0.5), 3061 (10.0), 3013 (0.8), 2962 (0.4), 2126 (0.4), 2100 (1.3), 2081 (1.0), 2055 (0.8), 2039 (0.2), 1591 (4.6), 1577 (1.3), 1440 (0.1), 1337 (1.0), 1276 (0.1), 1266 (0.1), 1186 (0.7), 1166 (0.6), 1114 (2.0), 1030 (2.5), 1002 (7.9), 730 (0.2), 666 (1.5), 618 (1.0), 492 (0.1), 417 (2.7), 391 (1.1), 371 (0.4), 314 (0.5), 281 (0.4), 270 (1.1), 239 (1.5), 201 (0.6) cm^{-1}; IR (KBr) 3077 (vw), 3058 (w), 3040 (vw), 3022 (vw), 2992 (vw), 2151 (vw, sh), 2142 (w), 2098 (s), 2079 (s), 2058 (s), 2037 (vs), 1588 (mw), 1573 (w), 1481 (m), 1437 (s), 1321 (s), 1304 (s), 1291 (s), 1270 (s), 1262 (s, sh), 1188 (w, sh), 1181 (mw), 1161 (w, sh), 1158 (w), 1115 (s), 1074 (vw), 1026 (w), 997 (mw), 925 (vw), 850 (w), 794 (w), 758 (m), 747 (m), 726 (s, sh), 724 (s), 693 (s), 665 (vw), 654 (vw), 616 (vw), 603 (vw), 588 (vw), 546 (s), 533 (s), 504 (s), 427 (w), 411 (w) cm^{-1}.

Crystal Structure Determinations. The single crystal X-ray diffraction data of $[PPh_4][As(N_3)_4]$ and $[PPh_4][Sb(N_3)_4]$ were collected on a Bruker SMART APEX 3-circle platform diffractometer, equipped with an APEX CCD detector with the χ-axis fixed at 54.74°, and using Mo K_α radiation (Graphite monochromator) from a fine-focus tube. The diffractometer was equipped with an LT-3 apparatus for low-temperature data collection using controlled liquid nitrogen boil off. A complete hemisphere of data was scanned on ω (0.3°) with a run time of 10-s per frame at a detector resolution of 512 × 512 pixels using the SMART software package.[13] A total of 1271 frames were collected in three sets and a final set of 50 frames, identical to the first 50 frames, was also collected to determine any crystal decay. The frames were then processed on a PC, running Windows 2000 software, by using the SAINT software package[13] to give the *hkl* files corrected for Lp/decay. The absorption correction was performed using the SADABS program.[13] The structures were solved by the Patterson Method using the SHELX-90 program and refined by the least-squares method on F^2, SHELXL-97 incorporated in SHELXTL Suite 6.12 for Windows NT/2000.[13] All non-hydrogen atoms were refined anisotropically.

The single crystal X-ray diffraction data of $[(Ph_3P)_2N][As(N_3)_4]$, $[NMe_4][Sb(N_3)_4]$, and $[(Ph_3P)_2N][Sb(N_3)_4]$ were collected on a Bruker SMART APEX DUO 3-circle platform diffractometer, equipped with an APEX II CCD detector with the χ-axis fixed at 54.74°, and using Mo K_α radiation (TRIUMPH curved-crystal monochromator) from a fine-focus tube. The diffractometer was equipped with an Oxford Cryostream 700 apparatus for low-temperature data collection. A complete hemisphere of data was scanned on ω (0.5°) with a run time of 1-s per frame at a detector resolution of 512 × 512 pixels using the BIS software package.[14] A total of 1464 frames was collected in four sets. The frames were then integrated using the SAINT algorithm[14] to give the *hkl* files corrected for Lp/decay. The absorption correction was performed using the SADABS program.[14] The structures were solved by the Direct Method and refined on F^2 using the Bruker SHELXTL Software Package.[14] All non-hydrogen atoms were refined anisotropically. ORTEP drawings were prepared using the ORTEP-3 for Windows V2.02 program.[15] Further crystallographic details can be obtained from the Cambridge Crystallographic Data Centre (CCDC, 12 Union Road, Cambridge CB21EZ, U.K. (Fax: (+44) 1223-336-033; e-mail: deposit@ccdc.cam.ac.uk) on quoting the deposition no. CCDC 844411−844415.).

Computational Methods. All calculations were performed using the recent hybrid meta exchange-correlation density functional M06-2X[16] in Gaussian 09, revision A.02.[17] M06-2X is a reliable general purpose density functional theory (DFT) functional for main-group chemistry, with a mean average deviation of ~2.2 kcal/mol, as demonstrated by several benchmarks.[16,18−20] We have recently verified its usefulness by accurately predicting the structures of some bismuth azides and iodine and bromine fluorides, for which other DFT methods, such as B3LYP, are known to perform poorly.[2]

In this work nitrogen atoms were described by the cc-pVTZ basis set,[21] whereas the heavier arsenic and antimony centers were treated by the cc-pwCVTZ-PP basis set.[22] The latter is based on a small-core relativistic Stuttgart pseudopotential that accurately recovers both scalar and spin−orbit relativistic effects of inner core electrons. It treats the valence and subvalence shells with a flexible triple-ζ Gaussian contraction to capture core−valence correlation effects.

Relative energies of anions in solutions were evaluated through the self-consistent reaction field approach, as implemented in the Solvent Model Density (SMD)[23] polarizable continuum (PCM) model in Gaussian 09. Some systems were also optimized with PCM, in which cases the smaller cc-pwCVDZ-PP basis set for arsenic and antimony and the corresponding cc-pVDZ basis set for nitrogen were used. Only minor changes from the gas-phase structures were observed in these cases.

The Hessian matrix was evaluated for all structures, to ensure that only minima on the potential energy surface were considered, and to provide vibrational frequencies. We have found only limited data on the accuracy of M06-2X for predicting vibrational frequencies. Predicted harmonic theoretical frequencies inherently differ from the observed fundamental frequencies, which include anharmonicity and mode−mode couplings. Therefore, empirical scaling of the predicted frequencies is necessary before direct comparisons can be made with the observed values. However, although we observe good agreement between our calculated spectra and experiment in general, we note that the empirical scaling required is unusually large, typically ~0.911 for the asymmetric azide stretching region (2000−2200 cm^{-1}) and ~0.915 for the entire spectral region (0−2200 cm^{-1}). Similarly large scaling factors were necessary both for calculations on gas-phase systems, as well as those described with implicit solvation through the SCRF-PCM approach. These scaling factors differ significantly from the 0.98 value initially recommended for the M06-2X functional.[16] For comparison we also calculated the spectra of several antimony and arsenic tetraazido anions at the B3LYP/cc-pwCVDZ-PP level. The B3LYP functional provided comparable results, albeit with an average scaling factor of ~0.95 for the azide antisymmetric stretching region (see the Supporting Information).

■ RESULTS AND DISCUSSION

Syntheses of the Arsenic and Antimony Polyazides. Anionic polyazides, $A^+_y[M(N_3)_{x+y}]^{y-}$ can be prepared by the reaction of ionic azides $A^+N_3^-$ with neutral polyazido compounds, $M(N_3)_x$.[2,6,11] The neutral polyazido compounds can be obtained from the corresponding covalent fluorides, MF_x, and Me_3SiN_3. In this work, salts with the tetraazidoarsenites, $[As(N_3)_4]^-$, and -antimonites, $[Sb(N_3)_4]^-$, were prepared in a one-step, quantitative synthesis from AsF_3 and SbF_3, respectively, by reaction with Me_3SiN_3 and a stoichiometric amount of the corresponding ionic azide AN_3 in acetonitrile solution (eq 1).

$$MF_3 + AN_3 + 3Me_3SiN_3 \xrightarrow{CH_3CN} A[M(N_3)_4] + 3Me_3SiF$$
$$M = As, Sb;\ A = NMe_4,\ PPh_4,\ (Ph_3P)_2N) \qquad (1)$$

This resulted in rapid and complete fluoride-azide exchange and easy product separation. All tetraazidopnictogen(+III) compounds were isolated as colorless and room-temperature stable materials. While tetramethylammonium tetraazidoarsenite, $NMe_4[As(N_3)_4]$, was a clear, colorless, viscous, ionic liquid at room temperature, all the other tetraazides were colorless crystalline solids. Because of the relatively high ionicity of their azido ligands and the presence of large counterions which diminish shock propagation, these compounds are less sensitive and explosive than the neutral parent compounds, $M(N_3)_3$, and during the course of our study could be manipulated at room temperature without explosions. The five crystalline tetraazidopnictogen(+III) salts were also investigated by DTA. The tetraazidoantimonites were found to be thermally more stable than the corresponding arsenites. While $[NMe_4][As(N_3)_4]$, $[PPh_4][As(N_3)_4]$, and $[(Ph_3P)_2N][As(N_3)_4]$ were found to have a decomposition onset at 75 °C, 87 °C, and 85 °C, respectively, $[NMe_4][Sb(N_3)_4]$, $[PPh_4][Sb(N_3)_4]$, and $[(Ph_3P)_2N][Sb(N_3)_4]$ started to decompose at higher temperatures of 204 °C, 202 °C, and 210 °C, respectively. This indicates that the nature of the counterion has little or no influence on the thermal stability of the tetraazidopnictogen(+III) compounds.

Crystal Structures. Crystal structures were determined for $[PPh_4][As(N_3)_4]$, $[(Ph_3P)_2N][As(N_3)_4]$, $[NMe_4][Sb(N_3)_4]$, $[PPh_4][Sb(N_3)_4]$, and $[(Ph_3P)_2N][Sb(N_3)_4]$. Selected crystallographic data for these structures are listed in Table 1.

$[PPh_4][As(N_3)_4]$. Our X-ray crystal structure of $[PPh_4][As(N_3)_4]$ is in good agreement with the previously published structure[10] and shows the presence of well isolated $[As(N_3)_4]^-$ anions and $[PPh_4]^+$ cations. The closest As···N and N···N contacts between neighboring anions are 5.60 Å and 3.31 Å, respectively. Figure 1A depicts the structure of the $[As(N_3)_4]^-$ anion in its $[PPh_4]^+$ salt. Selected bond lengths and angles of the anion are listed in Table 2. This structure approximates most

Table 1. Crystallographic Data for $[PPh_4][As(N_3)_4]$, $[(Ph_3P)_2N][As(N_3)_4]$, $[NMe_4][Sb(N_3)_4]$, $[PPh_4][Sb(N_3)_4]$, and $[(Ph_3P)_2N][Sb(N_3)_4]$

compound	$[PPh_4][As(N_3)_4]$	$[(Ph_3P)_2N][As(N_3)_4]$	$[NMe_4][Sb(N_3)_4]$	$[PPh_4][Sb(N_3)_4]$	$[(Ph_3P)_2N][Sb(N_3)_4]$
empirical formula	$C_{24}H_{20}AsN_{12}P$	$C_{36}H_{30}AsN_{13}P_2$	$C_4H_{12}N_{13}Sb$	$C_{24}H_{20}N_{12}PSb$	$C_{36}H_{30}N_{13}P_2Sb$
formula weight	582.41	781.58	364.02	629.24	828.42
temperature, K	163(2)	100(2)	100(2)	183(2)	100(2)
crystal system	monoclinic	triclinic	triclinic	monoclinic	triclinic
space group	C2	$P\bar{1}$	$P\bar{1}$	$P2_1/n$	$P\bar{1}$
a, Å	16.723(5)	10.223(10)	7.8125(1)	12.751(1)	10.3792(4)
b, Å	7.161(2)	10.642(10)	9.0472(1)	7.3433(8)	10.6043(4)
c, Å	11.702(3)	16.875(16)	9.9280(2)	27.749(3)	16.7458(7)
α, deg	90	95.375(12)	96.332(1)	90	95.1460(1)
β, deg	109.853(4)	94.219(13)	109.999(1)	91.411(2)	94.9940(1)
γ, deg	90	97.37(2)	98.009(1)	90	100.5720(1)
V, Å^3	1318.0(6)	1806.0(6)	644.15(2)	2597.4(5)	1794.4(1)
Z	2	2	2	4	2
ρ_{calc} g/cm^3	1.468	1.445	1.877	1.609	1.533
$F(000)$	592	800	356	1256	836
index ranges	$-20 \le h \le 21$, $-9 \le k \le 9$, $-14 \le l \le 10$	$-13 \le h \le 13$, $-14 \le k \le 14$, $-22 \le l \le 22$	$-11 \le h \le 10$, $-12 \le k \le 12$, $-14 \le l \le 14$	$-15 \le h \le 12$, $-8 \le k \le 9$, $-34 \le l \le 34$	$-14 \le h \le 14$, $-15 \le k \le 15$, $-23 \le l \le 23$
μ, mm^{-1}	1.389	1.083	2.151	1.163	0.906
crystal size, mm	0.15 × 0.09 × 0.05	0.34 × 0.28 × 0.25	0.51 × 0.31 × 0.31	0.22 × 0.06 × 0.05	0.20 × 0.19 × 0.09
no. of rflns. collect.	4625	32448	16956	15017	29102
no. of indep. rflns.	2846	8950	3898	5205	10971
R_{int}	0.0310	0.0314	0.0194	0.0713	0.0440
no. of params.	173	469	168	343	469
R1, $wR2$ $[I > 2\sigma(I)]$	0.0464, 0.0816	0.0273, 0.0645	0.0123, 0.0327	0.0487, 0.0785	0.0349, 0.0681
R1, $wR2$ (all data)	0.0667, 0.0890	0.0353, 0.0676	0.0126, 0.0329	0.0916, 0.0928	0.0544, 0.0746
$(\Delta/\rho)_{min/max}$, e Å^{-3}	0.434/−0.229	0.449/−0.368	0.763/−0.618	0.856/−0.486	0.504/−0.735

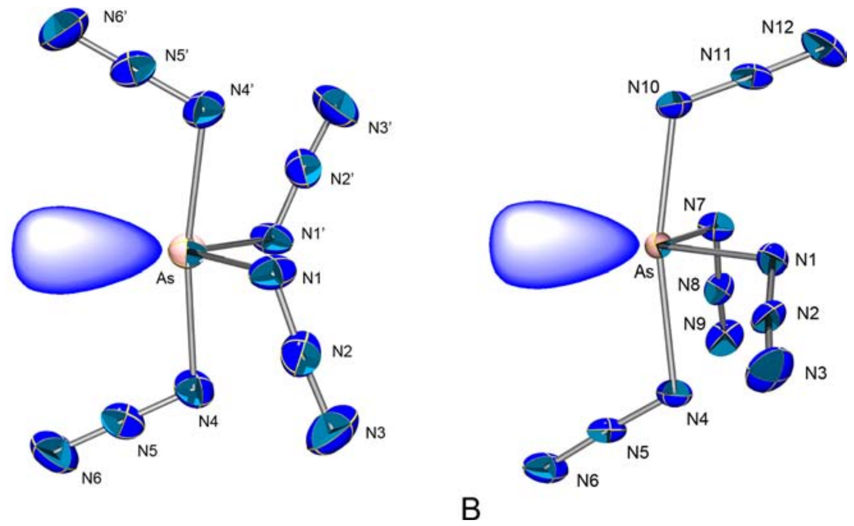

Figure 1. ORTEP plot for the anion in $[PPh_4][As(N_3)_4]$ (A) and $[(Ph_3P)_2N][As(N_3)_4]$ (B). The predicted, but unobserved, sterically active lone valence electron pair has been added to the ORTEP plot for a better understanding of the observed geometry. Thermal ellipsoids are drawn at the 30% probability level.

closely that of the total energy minimum of the free undisturbed $[As(N_3)_4]^-$ anion (**As-1**, see below).

If the formal lone valence electron pair at the arsenic atom is included, the structure can be derived from a trigonal bipyramid with the lone pair domain in an equatorial position which because of its greater space requirement compresses the axial N4−As−N4′ angle. In an ideal pseudo trigonal bipyramidal arrangement, the plane defined by the axial ligands and the lone pair bisects the angle between the equatorial ligands. Although the lone pair domain on the central atom cannot be observed directly in the crystal structure, its approximate location can be deduced from the observed geometry of the MN_4 skeleton, that is, from the orientation of the plane defined by the N_α atoms of the axial ligands and the central atom. When the lone pair domain is located on the C_2 axis, the plane defined by the two axial N_α atoms and the central atom, will bisect the equatorial MN_2 angle. This is the case for the $[PPh_4]^+$ salt of $[As(N_3)_4]^-$, predicting the presence of a lone pair domain on the C_2 axis.

$[(Ph_3P)_2N][As(N_3)_4]$. The crystal structure of the $[(Ph_3P)_2N]^+$-salt of the $[As(N_3)_4]^-$ anion also consists of isolated $[As(N_3)_4]^-$

Table 2. Selected Skeletal Bond Lengths [Å] and Angles [deg] for the Anions in $A[M(N_3)_4]$

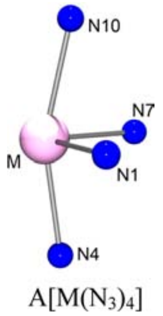

	A = [PPh4]; M = As	A = [(Ph3P)2N]; M = As	A = [NMe4]; M = Sb	A = [PPh4]; M = Sb	A = [(Ph3P)2N]; M = Sb
M−N1	1.888(4)	1.911(1)	2.1149(9)	2.078(4)	2.096(2)
M−N4	2.129(4)	2.201(1)	2.2616(9)	2.254(4)	2.240(2)
M−N7	1.888(4)	1.905(1)	2.1109(9)	2.071(4)	2.082(2)
M−N10	2.129(4)	2.047(1)	2.2635(9)	2.244(4)	2.280(2)
N1−M−N4	90.82(16)	83.42(5)	82.48(4)	84.12(16)	87.10(9)
N1−M−N7	97.2(2)	95.49(5)	96.26(4)	95.10(19)	93.22(8)
N1−M−N10	83.03(16)	87.19(5)	79.61(4)	77.96(17)	80.84(9)
N4−M−N7	83.03(16)	88.62(5)	81.67(3)	83.90(16)	82.14(7)
N4−M−N10	170.7(3)	167.62(5)	156.11(4)	154.96(16)	160.29(8)
N7−M−N10	90.82(16)	84.25(5)	84.70(4)	80.46(16)	83.03(8)
α[a]	0.3	−7.4	6.1	−4.5	5.2

[a] Angle between the plane defined by N4, As and N10 and the plane bisecting N1−As−N7. Positive values indicate a rotation toward N7, resulting in a rotation of the lone pair toward N1.

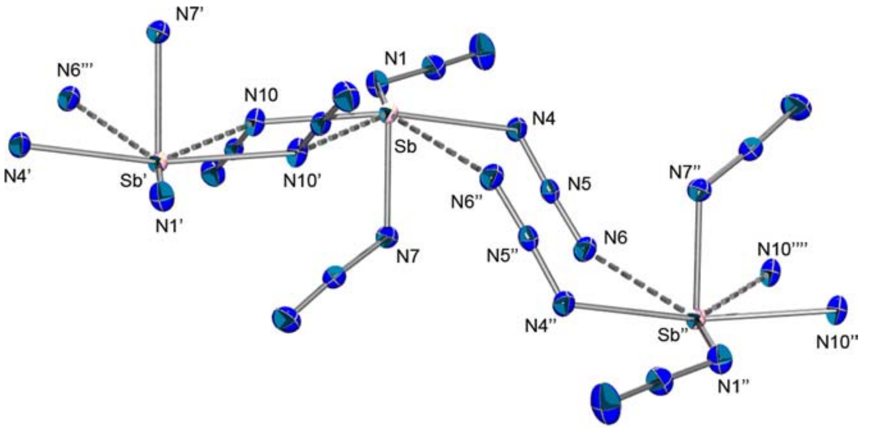

Figure 2. Chain structure of the $[Sb(N_3)_4]^-$ anion in $[NMe_4][Sb(N_3)_4]$. Thermal ellipsoids are shown at the 50% probability level. Selected bond lengths [Å] and angles [deg]: Sb−N4 2.262(1), Sb−N6″ 3.176(1), Sb−N10 2.263(1), Sb−N10′ 2.957(1) Sb″−N6 3.172(1), N4−Sb−N6″ 70.1(1), N10−Sb−N10′ 79.4(1), Sb−N10−Sb′ 114.5(1), Sb−N4−N5 120.4(1), Sb−N6″−N5″ 131.4(1).

and $[(Ph_3P)_2N]^+$ ions. Even though $[(Ph_3P)_2N]^+$ is larger than $[PPh_4]^+$, the $[As(N_3)_4]^-$ anions in $[(Ph_3P)_2N][As(N_3)_4]$ are packed closer to each other and the closest As···N and N···N contacts between neighboring anions are 3.78 Å and 3.34 Å, respectively. The compound crystallizes in the triclinic space group $P\bar{1}$. The structure of the $[As(N_3)_4]^-$ anion in its $[(Ph_3P)_2N]^+$-salt is depicted in Figure 1B, and selected bond lengths and angles are listed in Table 2. The structures of the anions in $[PPh_4][As(N_3)_4]$ and $[(Ph_3P)_2N][As(N_3)_4]$ are both derived from a trigonal bipyramid.

However, the azido ligands are oriented differently in the two salts. In the $[PPh_4]^+$-salt (Figure 1A), both axial azido ligands are oriented toward the lone pair domain. One equatorial N_3 group is pointing above the equatorial plane and the second one is pointing below the plane. In the $[(Ph_3P)_2N]^+$-salt (Figure 1B), only one of the axial azido ligands is oriented toward the lone pair domain, and the two equatorial N_3 ligands are oriented toward this ligand. The N1−As−N7 angle between the equatorial azido ligands is not bisected by the axial plane defined by N4, As, and N10. Instead, the plane is rotated to the side of N1 by about 7°. This leads to the conclusion that in $[(Ph_3P)_2N][As(N_3)_4]$ the center of the lone pair domain of arsenic is slightly tilted toward N7. The calculated energy difference between the two observed $[As(N_3)_4]^-$ conformations is only 0.4 kcal/mol, and the observation of two different structures can be attributed to minor differences in their respective lattice energies.

$[NMe_4][Sb(N_3)_4]$. This compound crystallizes in the triclinic space group $P\bar{1}$. Because of the smaller size of the $[NMe_4]^+$ counterion, the $[Sb(N_3)_4]^-$ anions are in close proximity to each other and form two Sb···N bridges with two neighboring anions which are shorter than the sum of the van der Waals (vdW) radii resulting in a chain structure (Figure 2). The chains are made up

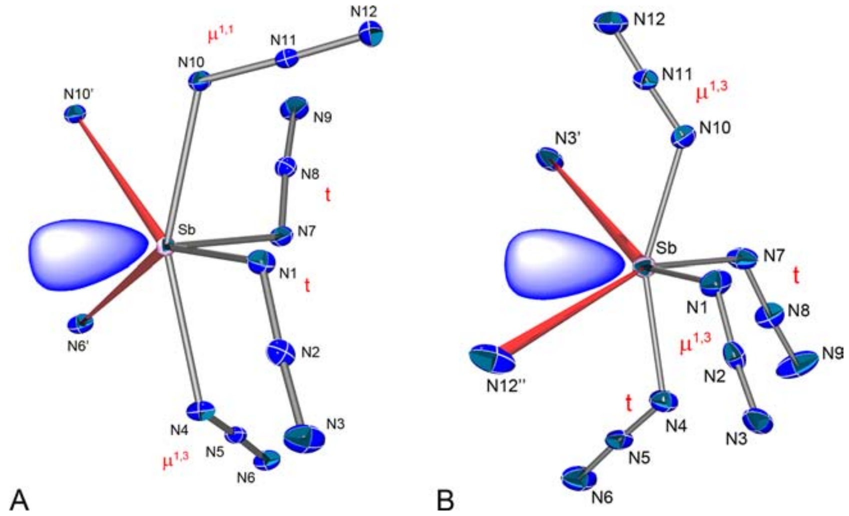

Figure 3. ORTEP plot of the isolated $[Sb(N_3)_4]^-$ units in $[NMe_4][Sb(N_3)_4]$ (A) and $[PPh_4][Sb(N_3)_4]$ (B) including the bridging nitrogen atoms from two neighboring $[Sb(N_3)_4]^-$ units. The red labels t and $\mu^{x,y}$ indicate the ligand types, terminal and bridging, respectively. Bridging bonds to neighboring units are drawn in red. Thermal ellipsoids are drawn at the 30% probability level. Again, the predicted lone pair domain has been added to the ORTEP plots for illustrative purposes.

from alternating planar four-membered Sb_2N_2 parallelograms, with two $\mu^{1,1}$-bridging N_3 ligands and chair-type eight-membered $Sb_2(N_3)_2$ rings with two $\mu^{1,3}$-bridging N_3 ligands.

The parallelograms result from two shorter (2.263(3) Å) and two longer (2.957(1) Å) Sb—N bonds and resemble those found in the $Sb(N_3)_3$ and $[PPh_4][Bi(N_3)_4]$ "Mitsubishi-type" structures.[2,4,8] The Sb—N bonds in the eight-membered rings have a length of 2.262(1) Å and 3.172(1) Å. A similar chain structure has previously been observed for the anion in $[PPh_4][Bi(N_3)_4]$[2,8] and the $(Py)_2Bi(N_3)_3$ adduct.[8] However, the structures of these bismuth compounds are quite different as they do not contain the eight-membered rings. In each isolated individual $[Sb(N_3)_4]^-$ unit of the chain, the formal lone valence electron pair at the antimony atom is sterically active. The location of the lone pair domain in $[NMe_4][Sb(N_3)_4]$ can be deduced from the following analysis. The close environment around each antimony atom consists of two terminal N_3 ligands (N1 and N7), one $\mu^{1,1}$-bridging N_3 ligand (N10), one $\mu^{1,3}$-bridging N_3 ligand (N4), and the sterically active Sb lone valence electron pair. This arrangement is derived from a pseudotrigonal bipyramid with the two terminal N_3 ligands and the formal lone valence electron pair in the three equatorial positions, and the two bridging N_3 groups occupying the two axial positions (Figure 3A). Both axial N_3 groups are bent away from the formal lone pair but are not coplanar; the dihedral angle between the two planes formed by N11, N10, N4 and N5, N6, N10 is 80.2(5)°. Because of the increased repulsion from the formal lone pair and the two long Sb—N bridges coming in from the same direction, the axial N4—Sb—N10 bond angle is compressed from the ideal 180° to 156.1(4)°. The equatorial N1—Sb—N7 angle is not bisected by the axial plane defined by N4, Sb, and N10. Instead, the plane is rotated to the side of N7 by about 6°. The ligand arrangement in $[Sb(N_3)_4]^-$ resembles somewhat that of the monomeric $EBiN_4$ skeleton in $[PPh_4][Bi(N_3)_4]$ with one equatorial azido group pointing up and the other one pointing down and the two axial N_3 groups being tilted away from the formal lone pair.[2,8]

When the two long nitrogen bridges from the two neighboring $[Sb(N_3)]_4^-$ units and the formal lone pair at the Sb atom are included in the coordination sphere, the coordination number of the antimony atom is increased to seven, and the observed ligand arrangement is an unusual motif for CN 7. In principle it is a strongly distorted trigonal bipyramid with two additional N-bridges coming in from above and below the equatorial plane and from the left of the plane formed by N10, Sb, and N4. The two bridges enhance the repulsion effect of the lone pair thus further compressing the axial and equatorial N—Sb—N angles. Selected bond length and angles for the $[Sb(N_3)_4]^-$ unit in $[NMe_4][Sb(N_3)_4]$ are listed in Table 2.

It should be noted that according to the official nomenclature conventions, the coordination number is determined exclusively by the number of ligands, and, therefore, sterically active lone pairs are not included in the coordination number. In this paper, the sterically active lone pairs have been included in the CN to facilitate the rationalization of the observed geometries and the term "formal coordination number" has been used to describe this situation.

$[PPh_4][Sb(N_3)_4]$. Our X-ray crystal structure of $[PPh_4][Sb(N_3)_4]$ is in good agreement with the previously published structure.[10] As in the $[N(CH_3)_4]^+$ salt, the $[Sb(N_3)_4]^-$ units are in close proximity to each other and form two Sb···N bridges, with two neighboring anions which are shorter than the sum of the vdW radii. While in the $[NMe_4]^+$-salt the two azido bridges, one $\mu^{1,1}$ and one $\mu^{1,3}$, involve the two axial ligands and result in a chain structure, in the $[PPh_4]^+$-salt both bridges are $\mu^{1,3}$ bridges and involve one axial and one equatorial N_3 group. The $[Sb(N_3)_4]^-$ units are interconnected through the azido bridges resulting in a helical chain structure (Figure 4) for the anion in $[PPh_4][Sb(N_3)_4]$ which are aligned along the [010] direction of the crystal.

As in the $[NMe_4]^+$-salt, the basic geometry of the $[Sb(N_3)_4]^-$ unit in the $[PPh_4]^+$-salt is derived from a pseudotrigonal bipyramid with one terminal N_3 ligand (N7), one $\mu^{1,3}$ bridging N_3 ligand (N1) and the sterically active formal lone pair being located at the three equatorial positions, and a terminal (N4) and a $\mu^{1,3}$ bridging (N10) N_3 group occupying the two axial positions (Figure 3B). The axial N—Sb—N bond angle is compressed from the ideal 180° to 155.0(2)° by the more space demanding lone pair and two Sb···N bridges. While the basic geometry of the SbN_4 skeleton is the same for $[NMe_4][Sb(N_3)_4]$ and $[PPh_4][Sb(N_3)_4]$, the arrangement of the ligands is different. In the

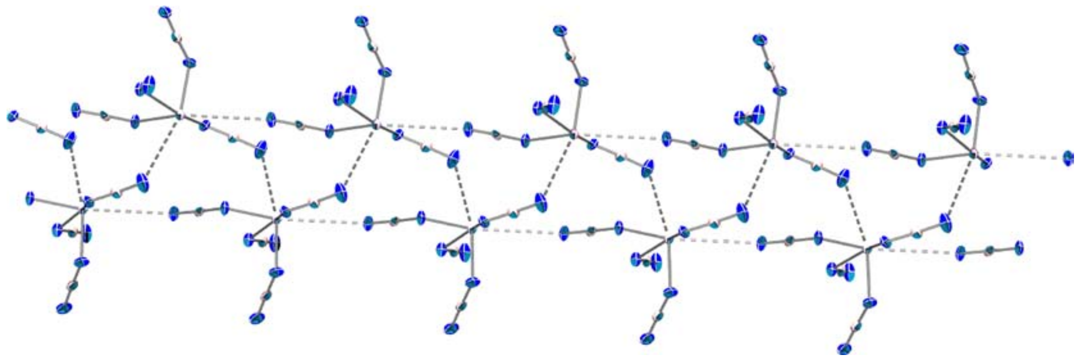

Figure 4. Part of the chain structure of the $[Sb(N_3)_4]^-$ anion in $[PPh_4][Sb(N_3)_4]$ in the [010] direction of the crystal. Thermal ellipsoids are shown at the 30% probability level.

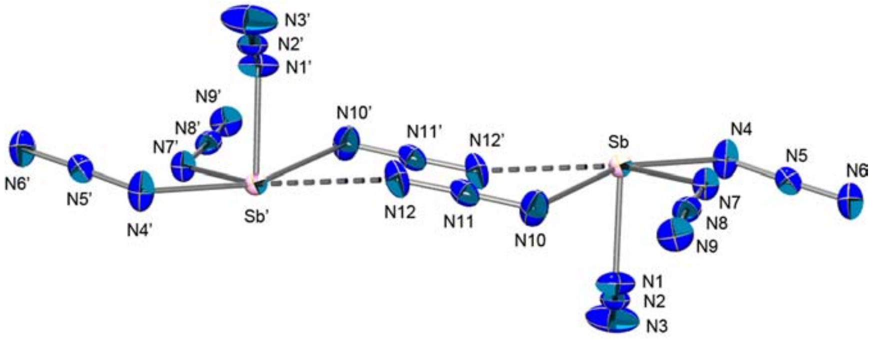

Figure 5. Dimeric structure of the $[Sb(N_3)_4]^-$ anion in the crystal of $[(Ph_3P)_2N][Sb(N_3)_4]$. Thermal ellipsoids are shown at the 50% probability level. Selected bond lengths [Å] and angles [deg]: Sb—N10 2.280(2), Sb—N12′ 3.024(2), N10—Sb—N12′ 81.6(1), Sb—N10—N11 112.9(1), Sb—N12′—N11′ 145.0(1).

$[NMe_4]^+$-salt, one equatorial N_3 group is pointing up and the other one is pointing down while both axial N_3 groups are tilted away from the lone pair domain, are not coplanar, and are bridging (Figure 3A). In the $[PPh_4]^+$-salt, both equatorial N_3 groups are pointing below the equatorial plane, and both axial N_3 groups are tilted toward the lone pair. The two bridging azido groups involve one equatorial (N1) and one axial (N10) ligand (Figure 3B). In addition, both axial N_3 groups are virtually coplanar with an angle of less than 1° between the planes defined by N11, N10, N4 and N5, N4, N10. Again, the equatorial N1—Sb—N7 angle is not bisected by the axial plane defined by N4, Sb, and N10. Instead, the plane is rotated to the side of N1 by about 5°. This results in a slight rotation of the antimony lone pair domain toward N7. This different arrangement results in the formation of a helical chain anion structure.

$[(Ph_3P)_2N][Sb(N_3)_4]$. The $[(Ph_3P)_2N]^+$-salt crystallizes in the triclinic space group $P\overline{1}$ with two formula units in the unit cell ($Z = 2$). Again, the $[Sb(N_3)_4]^-$ anions are not isolated units but form isolated Sb···N bridged dimers. In each dimer, two $[Sb(N_3)_4]^-$ units, that are related through a center of symmetry, are linked through two $\mu^{1,3}$-azido bridges (Figure 5). These N_3-bridges together with the two Sb atoms form an eight-membered $[Sb_2(N_3)_2]$ ring in a flattened chair conformation. While each Sb atom in the $[NMe_4]^+$ and $[PPh_4]^+$-salts forms two Sb···N bridges resulting in a polymeric anion structure with a "formal coordination number" of seven, in the $[(Ph_3P)_2N]^+$-salt each Sb atom forms only one Sb···N bridge, resulting in a dimeric structure with a "formal coordination number" of six. The shortest Sb···N distances between different dimers are 6.965 Å. The formation of dimeric anion units is probably due to the higher steric demand of the $[(Ph_3P)_2N]^+$-counterion compared to $[PPh_4]^+$ and renders the formation of a polymeric anion chain less favorable. Again, the geometry of the SbN_4 skeleton in the $[(Ph_3P)_2N]^+$-salt is derived from a pseudotrigonal bipyramid with two terminal N_3 ligands and the sterically active formal lone valence electron pair occupying the three equatorial positions

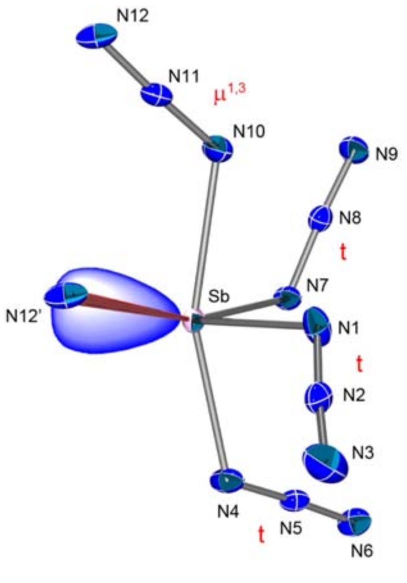

Figure 6. ORTEP plot of the anion in $[(Ph_3P)_2N][Sb(N_3)_4]$ including the bridging nitrogen atom N12′ from the neighboring $[Sb(N_3)_4]^-$ unit. Thermal ellipsoids are drawn at the 30% probability level. The red labels t and $\mu^{1,3}$ indicate terminal and $\mu^{1,3}$ bridging ligands, respectively. The bridging bond Sb—N12′ is 3.024(2) Å long. The unobserved formal lone pair has been added for illustrative purposes.

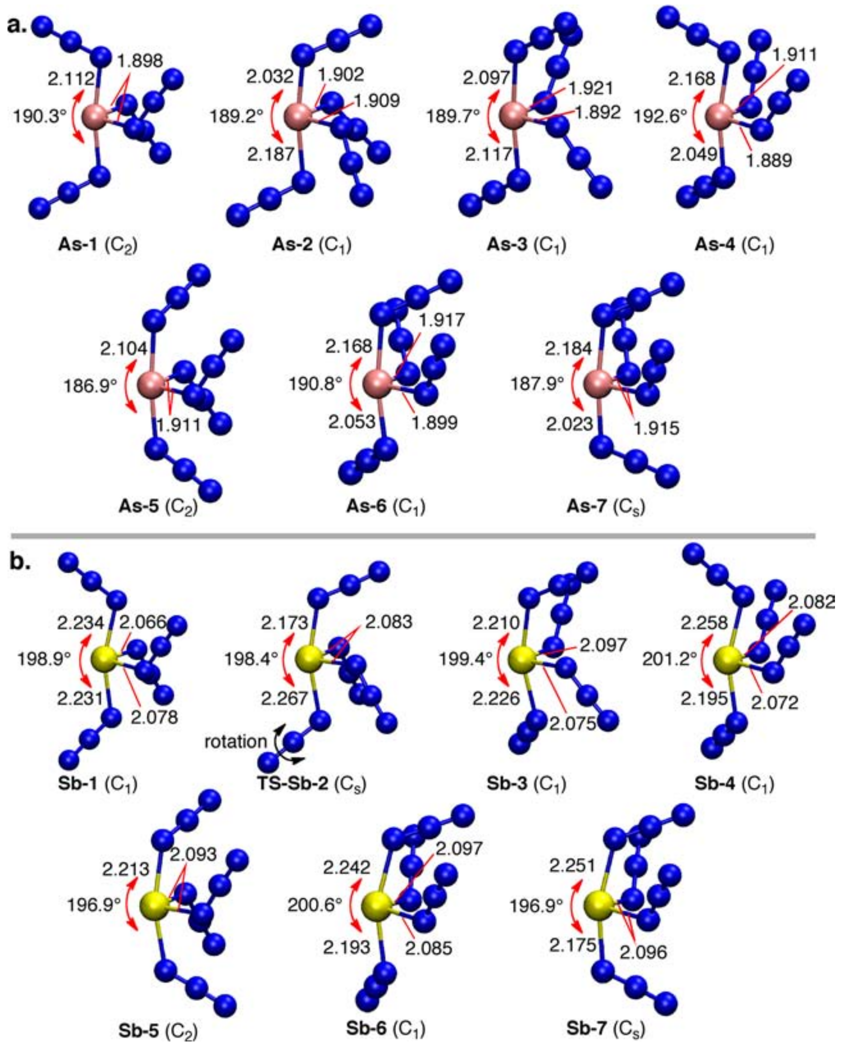

Figure 7. Calculated gas-phase geometries and symmetries of the major conformers of (**a**) $[As(N_3)_4]^-$ and (**b**) $[Sb(N_3)_4]^-$. Bond lengths are given in Å.

(Figure 6). One terminal and the bridging N_3 group occupy the two axial positions and are virtually coplanar. The angle between the two planes formed by N5, N4, Sb and N11, N10, Sb is less than 1°. The axial N4−Sb−N10 bond angle is compressed from the ideal 180° to 160.3(1)°, and the equatorial N1−Sb−N7 angle is compressed to 93.2(1)° from the ideal 120°. The bridging axial N_3 ligand points toward the formal lone pair while the terminal one points away from it. Of the two equatorial ligands, one points up and one points down. Thus, the ligand arrangement in the $[(Ph_3P)_2N]^+$-salt is again different from those observed in the other salts. The axial plane defined by N4, Sb, and N10 is rotated to the side of N7 by about 5° and does not bisect the equatorial N1−Sb−N7 angle. This results in a slight rotation of the antimony lone pair domain toward N1.

When the additional long nitrogen bridge to N12′ of the second $[Sb(N_3)_4]^-$ unit of the dimer is included in the coordination sphere, the "formal coordination number" is six. This bridge is pointing above the equatorial plane formed by N1−Sb−N7 of the $[Sb(N_3)_4]^-$ unit (Figure 6). Selected bond lengths and angles for the $[Sb(N_3)_4]^-$ unit in $[(Ph_3P)_2N][Sb(N_3)_4]$ are summarized in Table 2.

Conformational Variability. This series of $[M(N_3)_4]^-$ (M = As and Sb) structures is highly unusual because five different conformers were found for five different salts. Although all anions possess the same MN_4E (E = formal lone pair domain of M) skeleton, the arrangement of the azido ligands in each anion is completely different. To our best knowledge, such a great variability of conformers is unprecedented in inorganic main group chemistry. In the following theoretical section we have analyzed each conformer in detail to rationalize the multitude of observed structures, and to facilitate the analysis of the solid-state and solution vibrational spectra. The observation of extraordinary conformational variability for these anions can be attributed to the high fluxionality of the azido ligands as demonstrated by the presence of many low-frequency torsional modes (see Supporting Information). The big surprise was our ability to isolate and characterize, in spite of their very small energy differences, each conformer in pure form in the solid state.

Computational Results. To quantify the fluxionality of the tetraazido-antimony and -arsenic anions, we calculated the gas-phase energies and structures of all the seven possible major conformations (Figure 7) at the M06-2X/cc-pwCVTZ-PP level of theory, that is, all combinations of axial ligands pointing to the "front and back", and equatorial ligands pointing "up and down". Conformers **1**−**5** were optimized from their closest experimental X-ray crystal structure analogues, whereas the starting geometries for the experimentally unobserved conformers **6** and **7** were obtained through rotation of one axial azido ligand of conformers **4** and **2**, respectively. This was followed by solution energy calculations at the SMD-PCM-M06-2X/cc-pwCVTZ-PP level.

Table 3. Relative Energies (in kcal/mol) of All Considered Conformers at the M06-2X/cc-pwCVTZ-PP Level of Theory[a]

	$As(N_3)_4^-$		$Sb(N_3)_4^-$	
conformer:	ΔH^0	ΔG^0	ΔH^0	ΔG^0
1[b]	0.0 (0.0)	0.0 (0.0)	0.0 (0.0)	0.0 (0.0)
2	−1.1 (−1.2)	−0.4 (−0.5)	−1.3 (−2.2)[c]	0.7 (0.4)[c]
3	−0.2 (−0.6)	0.4 (0.0)	−0.7 (−1.2)	0.1 (−0.5)
4	0.1 (−0.1)	0.4 (0.2)	0.1 (−0.4)	0.7 (0.2)
5[b]	0.1 (−0.8)	2.0 (1.0)	−1.0 (−2.2)	0.7 (−0.4)
6	2.4 (0.4)	3.9 (1.9)	1.4 (−0.6)	2.6 (0.7)
7	1.6 (−0.4)	3.1 (1.1)	0.4 (−1.4)	1.7 (−0.2)
[3−2]			31.0 (−10.2)	43.9 (0.7)
[3−3]			31.6 (−7.8)	43.7 (2.4)

[a] Values for acetonitrile (1M, 298 K) are given in parentheses. [b] Two enantiomers. [c] Transition state corresponding to rotation of one axial azido ligand.

Because of the great similarity of the different conformers, inherent errors in the DFT method should largely cancel out. Therefore, we can expect a high precision in relative energies, considerably better than the method's already good general accuracy of ~2.2 kcal/mol[3].

The conformers of $[As(N_3)_4]^-$ are shown in Figure 7a and their relative energies are listed in Table 3. Not surprisingly, the conformers are very close in energy. Indeed, **As-1−4** are so close ($\Delta G^0 < \sim 0.5$ kcal/mol), that we can expect rapid interconversion in solution. Conformers **As-5−7** lie 1.5−2.5 kcal/mol higher in energy relative to the lowest conformer **As-2**, and should have a negligible contribution to the overall population.

In contrast to the equilibrium cases in solution, the single crystals of each compound contain only one conformer showing small thermal ellipsoids and no disorder. We note that the two conformers predicted to have *marginally* lower energy (**As-1** and **As-2**) in the gas-phase are the ones also observed experimentally in the $[PPh_4]^+$ and $[(Ph_3P)_2N]^+$-salts, respectively.

The analogous seven monomeric conformers (**Sb-1−7**) of $[Sb(N_3)_4]^-$ are shown in Figure 7b and are closely related to their arsenic analogues, except **Sb-2**, which is a transition state of C_s symmetry. Despite several attempts, no local minimum corresponding to **Sb-2** was found. This is likely due to a very shallow potential energy surface, and does not affect our conclusions.

The antimony conformers proved closer in energy compared to their arsenic analogues, with **Sb-2** and **Sb-6** being the least favorable by a slight margin (Table 3). However, because all the antimony salts proved dimeric or polymeric experimentally, we also investigated two conformers of the dimer $[(Sb(N_3)_4)_2]^{2-}$, [**Sb-3−Sb-2**] and [**Sb-3**]$_2$, which resulted after optimization from our X-ray structures (Figure 8). Presumably, the tendency of the azidoantimonites to associate arises from the larger antimony atom seeking higher coordination numbers. Since dimers and extended chains require sharing of bridging azide ligands for their formation, conformers **2** and **3** appear ideally suited for this purpose.

For the considered systems, the entropic cost of dimer formation, because of lowered vibrational, rotational, and translational degrees of freedom, is approximately 11−13 kcal/mol at ambient temperature. In addition, there exists a significant Coulombic penalty when combining two negatively charged species. Together, these effects prevent the formation of extended systems in the gas-phase. However, solvated and solid-state systems are markedly different, and surrounding solvent molecules and crystal lattice fields can greatly affect and govern which structures are formed. Whereas the Gibbs free energy penalty for forming dimeric $[Sb(N_3)_4]^-$ units in the gas-phase is a staggering 44 kcal/mol, the existence of such species in solution or solid state is more likely. Optimization of [**Sb-3−Sb-2**] in the implicit reaction field of acetonitrile (SMD-PCM) revealed the relative enthalpy of binding to be −10 kcal/mol. This value completely counteracts the entropic penalty, and the free energy of binding is close to zero (at 1 M and 298 K). In other words, we can expect a mixture of dimers and monomers in polar solvents. If dimers are present in solution, it is possible that they could aggregate further into larger systems, which subsequently could nucleate into crystals. Thus, such a dynamic case might explain why $[Sb(N_3)_4]^-$ salts crystallize as various extended systems, whereas $[As(N_3)_4]^-$ salts do not.

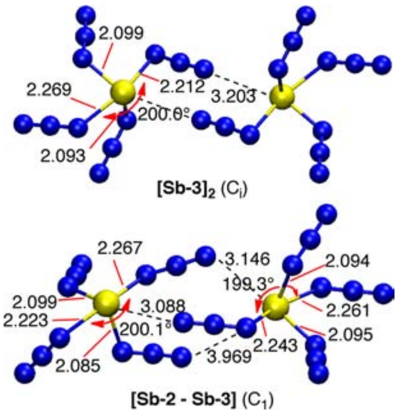

Figure 8. Calculated gas-phase geometries and symmetries of two $[(Sb(N_3)_4)_2]^{2-}$ conformers. Bond lengths are given in Å.

Because barriers to azide rotation are small, the interconversion of conformers in solution will be extremely fast, and on the time scale of molecular vibrations. Therefore, the dynamic equilibrium is too fast for NMR measurements and might only be accessible by means of vibrational spectroscopy.

Vibrational Spectra. Raman spectra of the solids and CH_3CN and SO_2 solutions and infrared spectra of the solids were recorded for all compounds (Figures 9−13, Experimental Section, and Supporting Information). The calculated vibrational spectra for all free, gaseous conformers are given in Figures 14−16, and the Supporting Information.

An analysis of the observed Raman spectra allows the following conclusions. (1) Since the pseudotrigonal bipyramidal EMN_4 (E = formal lone pair domain of M) skeletons are very similar for all the conformers, the skeletal modes are not very useful for distinguishing the different conformers. However, the frequencies, relative intensities, and number of observed bands of

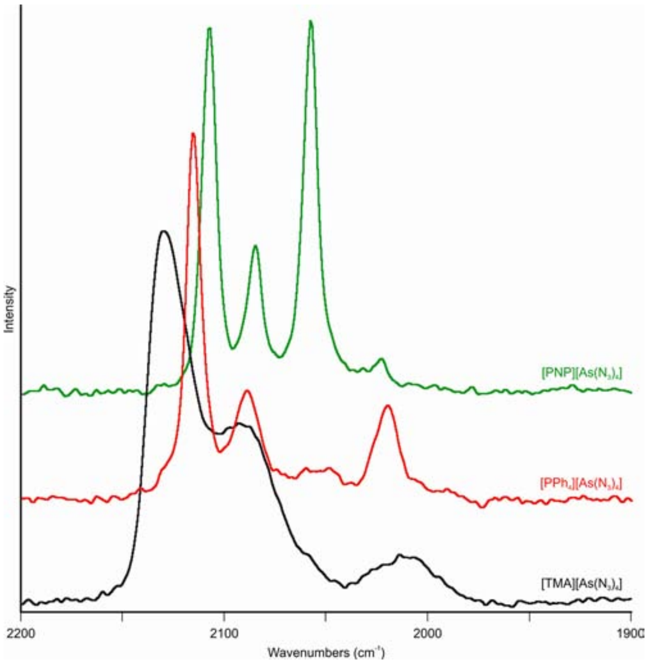

Figure 9. Azide antisymmetric stretching regions in the Raman spectra of liquid $[NMe_4][As(N_3)_4]$ (broad bands due to rapidly exchanging equilibrium of several conformers) and solid $[PPh_4][As(N_3)_4]$ and $[(Ph_3P)_2N][As(N_3)_4]$ (narrower bands due to well isolated ions with different ligand arrangements).

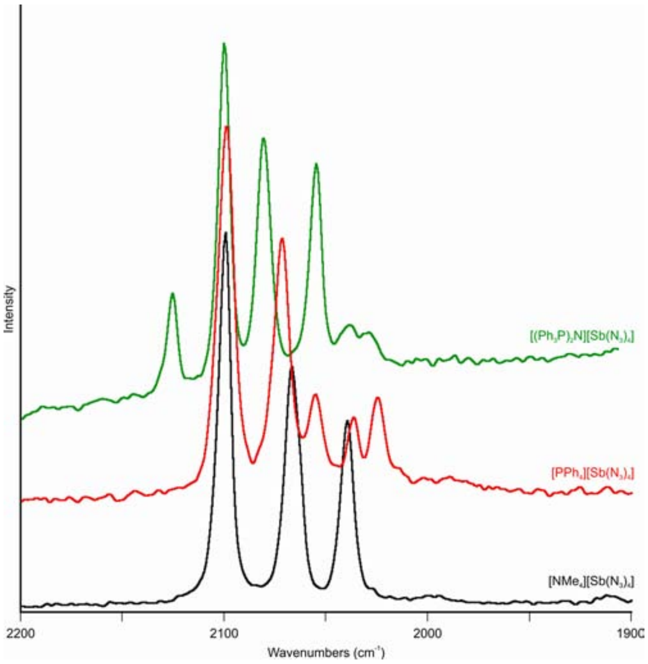

Figure 10. Azide antisymmetric stretching regions in the Raman spectra of solid $[NMe_4][Sb(N_3)_4]$ (infinite chains with alternating Sb_2N_2 parallelograms and eight-membered $Sb_2(N_3)_2$ rings), $[PPh_4][Sb(N_3)_4]$ (helical chains with $\mu^{1,3}$ bridges), and $[(Ph_3P)_2N][Sb(N_3)_4]$ (dimeric anion with an eight-membered $Sb_2(N_3)_2$ ring).

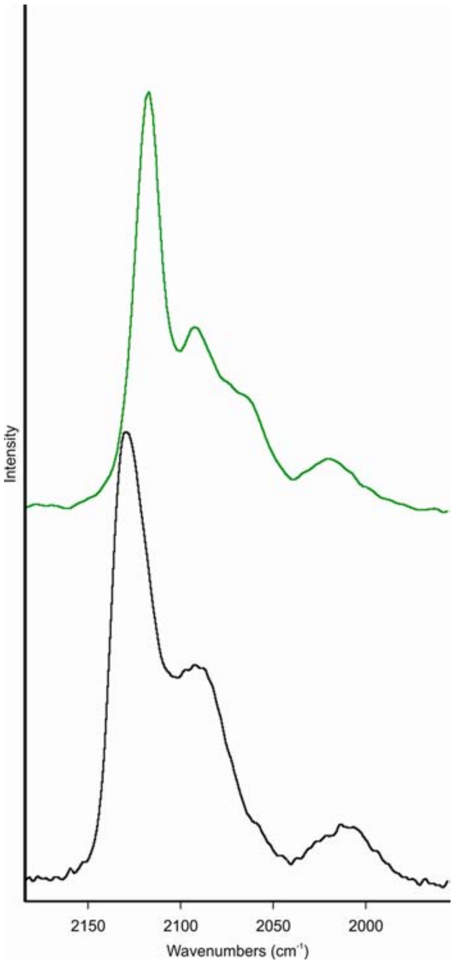

Figure 11. Azide antisymmetric stretching region in the Raman spectra of liquid $[NMe_4][As(N_3)_4]$ (black) and its CH_3CN solution at −30 °C (green).

the antisymmetric stretching vibrations of the azido ligands are strongly influenced by the ligand arrangements and occur in a region which is not obscured by cation or solvent bands. Therefore, they are ideally suited for characterizing the different conformers. As can be seen from Figures 9 and 10, the five solid $[M(N_3)_4]^-$-salts exhibit very distinct, well resolved, characteristic patterns. Not surprisingly, the ionic-liquid, $[NMe_4][As(N_3)_4]$, exhibits broader bands and a spectrum almost identical to that observed for its CH_3CN solution (Figure 11), suggesting the simultaneous presence of multiple conformers. The presence of multiple conformers also explains our failure to obtain a crystal structure for this compound; (2) the Raman bands for the CH_3CN and SO_2 solutions are different and much broader than those of the solids and very similar for $[PPh_4][As(N_3)_4]$ (Figure 12) and $[(Ph_3P)_2N][As(N_3)_4]$ (Supporting Information, Figure S22), demonstrating that the anion structures are no longer governed by the cation and that the solution spectra are due to rapidly exchanging multiple conformers. It is also noteworthy that the spectra are solvent dependent, that is, differ significantly for the CH_3CN and SO_2 solutions, implying different solvent interactions and/or conformer equilibria. Because of the relatively low solubility of these salts, the signal-to-noise ratio of the solution spectra is somewhat poor but sufficient to demonstrate the above points; (3) the $[PPh_4]^+$ (Figure 13), $[NMe_4]^+$ (Supporting Information, Figure S23) and $[(Ph_3P)_2N]^+$-salts (Supporting Information, Figure S24) of $[Sb(N_3)_4]^-$ behave similarly to the arsenic analogues when dissolved in CH_3CN or SO_2 but, as expected, their spectra are somewhat different from those of the As salts. Contrary to $[NMe_4][As(N_3)_4]$, the $[NMe_4][Sb(N_3)_4]$ salt is solid at room temperature and contains a well-ordered, single conformer, polymeric anion which, in spite

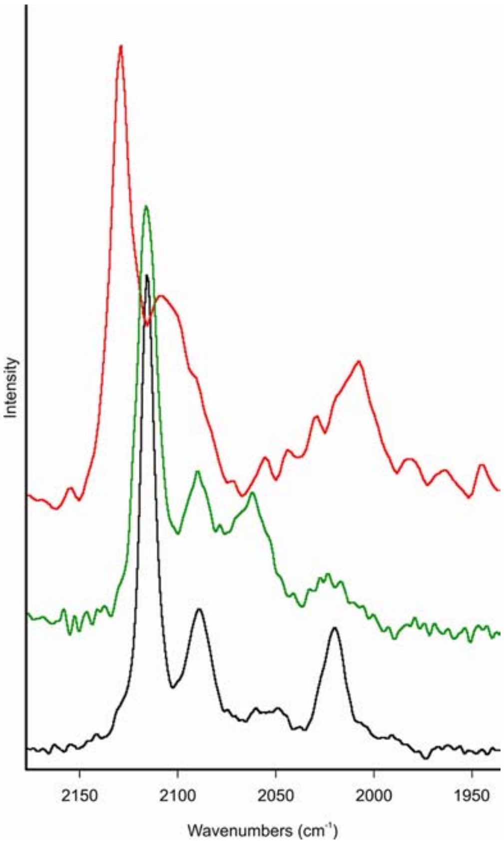

Figure 12. Azide antisymmetric stretching region in the Raman spectra of $[PPh_4][As(N_3)_4]$: neat solid (black), CH_3CN solution at −30 °C (green), and SO_2 solution at −30 °C (red).

of the presence of two different kinds of azido bridges, gives rise to a surprisingly simple Raman spectrum (Figure 10 and Supporting Information, Figure S23); and (4) freezing of the CH_3CN solutions at −80 °C did not dramatically change the spectra from those recorded for the solutions at −30 °C.

As one might expect from the fact that only the solid $[As(N_3)_4]^-$ salts contain single, well isolated, monomeric conformers, the agreement between the observed solid-state and calculated theoretical data is best for the arsenic compounds. Figure 14 shows the calculated gas-phase Raman spectrum of **As-1** together with the solid-state spectrum of $[PPh_4][As(N_3)_4]$ in the azide antisymmetric stretching region, 2000−2140 cm^{-1}. Four characteristic bands, corresponding to the axial and equatorial in- and out-of-phase stretching modes, show that the ions are not markedly perturbed by the presence of a solid lattice.

In solution multiple structures are in rapid equilibrium, and identification of individual conformers is challenging. With the exception of the axial in-phase vibrations most azide stretching modes differ only slightly between each conformer. Fortunately, our calculations show that the corresponding Raman intensities can vary significantly, thus enabling a more quantitative fingerprinting of experimental spectra (Figure 15). For example, a relatively small increase in the contribution from **As-2** is in principle sufficient to explain the major difference in the intensity patterns of $[PPh_4][As(N_3)_4]$ in acetonitrile and SO_2 solutions (Figure 12). In an effort to model the Raman spectrum of $[PPh_4][As(N_3)_4]$ in acetonitrile solution, which arises from a complex equilibrium, nine theoretical spectra (seven conformers and two enantiomers of **As-1** and **As-5**) were weighted in a

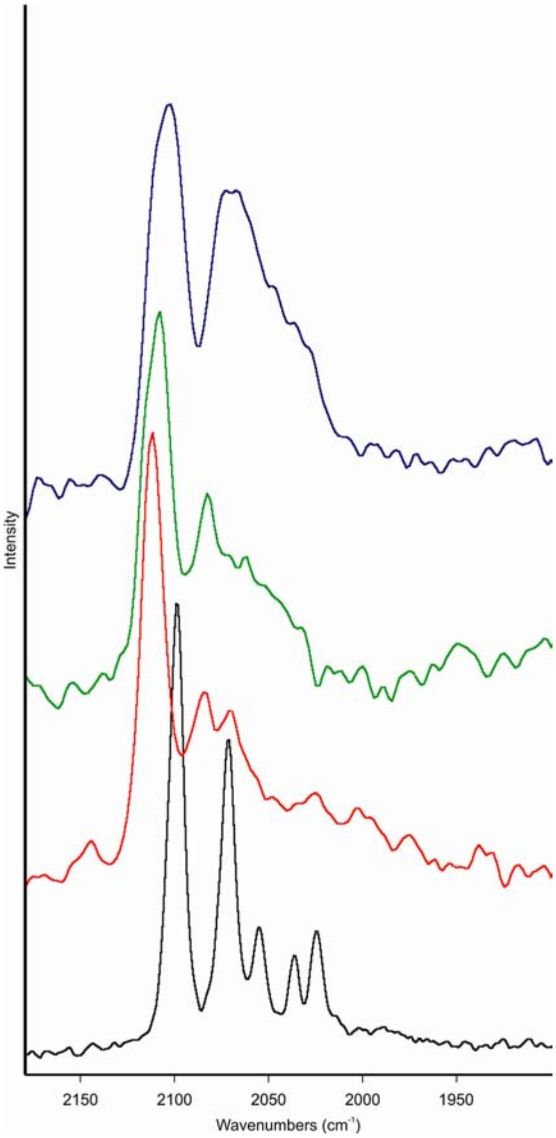

Figure 13. Azide antisymmetric stretching region in the Raman spectra of $[PPh_4][Sb(N_3)_4]$: neat solid (black), SO_2 solution at −30 °C (red), CH_3CN solution at −30 °C (green), frozen CH_3CN solution at −80 °C (blue).

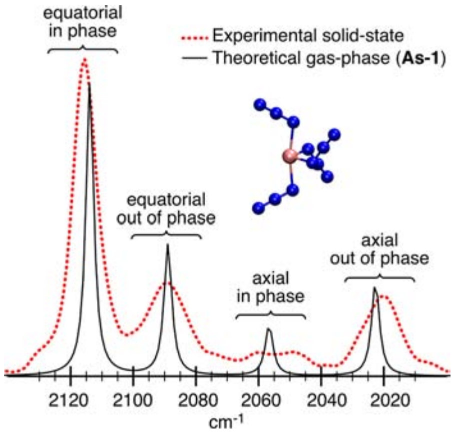

Figure 14. Experimental solid-state $[PPh_4][As(N_3)_4]$ (dotted line) and theoretical $[As(N_3)_4]^-$ (solid line) Raman spectra in the azide antisymmetric stretching region.

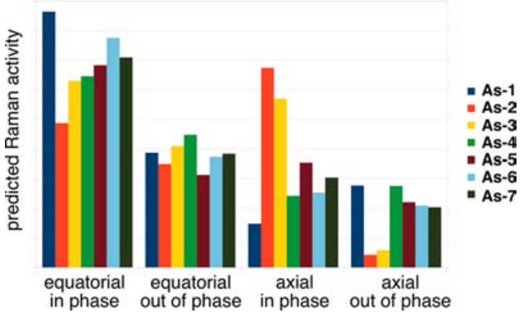

Figure 15. Theoretical Raman intensity patterns of the azide antisymmetric stretching modes of the seven $[As(N_3)_4]^-$ conformers.

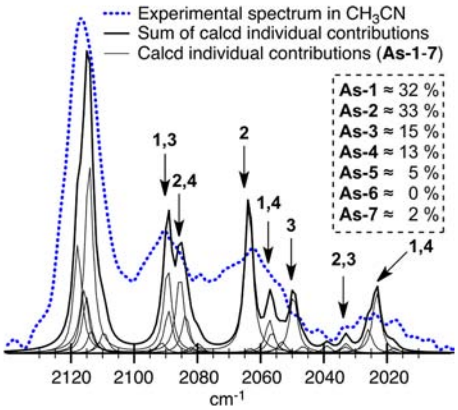

Figure 16. Experimental spectrum of a solution of $[PPh_4][As(N_3)_4]$ in CH_3CN (−30 °C, dotted line) and theoretical Raman spectra of the different $[As(N_3)_4]^-$ conformers (solid line) in the azide antisymmetric stretching region. The inset shows the predicted populations of the individual conformers at −30 °C in acetonitrile solution.

Boltzmann distribution at −30 °C (Figure 16). The procedure successfully explains the observed line broadening and the overall intensity pattern.

Spectra of the antimony compounds in solution are more complex because of a higher number of populated monomeric conformers, polyanions, as well as the presence of bridging ligands. Consequently, they were not analyzed in further detail.

■ CONCLUSIONS

A systematic experimental and theoretical study of the structures of the $[NMe_4]^+$, $[PPh_4]^+$, and $[(Ph_3P)_2N]^+$ salts of the tetraazidoarsenite and tetraazidoantimonite anions demonstrates that in highly fluxional species possessing numerous minimum energy structures of very similar energies and low barriers for their interconversion, subtle changes in solid-state effects can result in very different, well-defined, ordered anion structures. Thus, for five similar salts five different structures were experimentally observed in the solid state providing a text book example for the existence of conformational variability in inorganic main group chemistry. It is shown that very small changes in packing energies and cation−anion interactions can give rise to different anion structures, reminding us of chameleons which can adapt their colors to small changes in their environment. In solution, multiple conformers can exist, undergoing facile interconversion resulting in averaged, solvent dependent fluxional structures. Therefore, for highly fluxional compounds, such as polyazides, great care must be exercised with conclusions concerning structural principles and a preferred structure based on the observed experimental geometry of a single salt.

■ ASSOCIATED CONTENT

Ⓢ Supporting Information

Figures S1−S25 and Tables S1−S29. This material is available free of charge via the Internet at http://pubs.acs.org.

■ AUTHOR INFORMATION

Corresponding Author

*E-mail: haiges@usc.edu (R.H.), kchriste@usc.edu (K.O.C.).

Notes

The authors declare no competing financial interest.

■ ACKNOWLEDGMENTS

This work was supported by the National Science Foundation, the Office of Naval Research, the Air Force Office of Scientific Research, the Defense Threat Reduction Agency, and the Department of Energy. We appreciate the NSF CRIF Grant 1048807 to support an X-ray diffractometer. Computational work at USC was supported by the University of Southern California Center for High-Performance Computing and Communications. M.R. is grateful for financial support from the Swedish Research Council (VR).

■ DEDICATION

Dedicated to Professor George Olah on the occasion of his 85th birthday.

■ REFERENCES

(1) Klapoetke, T. M.; Tornieporth-Oetting, I. C. *Nichtmetallchemie*; VCH: Weinheim, Germany, 1994; p 283.

(2) Haiges, R.; Rahm, M.; Dixon, D. A.; Garner, E. B.; Christe, K. O. *Inorg. Chem.* **2012**, *51*, 1127 , and references cited therein.

(3) (a) Buder, W.; Schmidt, A. *Z. Anorg. Allg. Chem.* **1975**, *415*, 263. (b) Volgnandt, P.; Schmidt, A. *Z. Anorg. Allg. Chem.* **1976**, *425*, 189. (c) Portius, P.; Fowler, P. W.; Adams, H.; Todorova, T. Z. *Inorg. Chem.* **2008**, *47*, 12004. (d) Klapötke, T. M.; Geissler, P. *J. Chem. Soc., Dalton Trans.* **1995**, 3365. (e) Geissler, P.; Klapötke, T. M. *Spectrochim. Acta, Part A* **1995**, *51*, 1075. (f) Klapötke, T. M.; Nöth, H.; Schuett, T.; Warchhold, M. *Angew. Chem., Int. Ed.* **2000**, *39*, 2108. (g) Klapötke, T. M.; Schulz, A.; McNamara, A. *J. Chem. Soc., Dalton Trans.* **1996**, 2985.

(4) Haiges, R.; Vij, A.; Boatz, J. A.; Schneider, S.; Schroer, T.; Gerken, M.; Christe, K. O. *Chem.—Eur. J.* **2004**, *10*, 508.

(5) Karaghiosoff, K.; Klapötke, T. M.; Krumm, B.; Nöth, H.; Schütt, T.; Suter, M. *Inorg. Chem.* **2002**, *41*, 170.

(6) Haiges, R.; Boatz, J. A.; Vij, A.; Vij, V.; Gerken, M.; Schneider, S.; Schroer, T.; Yousufuddin, M.; Christe, K. O. *Angew. Chem., Int. Ed.* **2004**, *43*, 6676.

(7) Lyhs, B.; Jansen, G.; Blaeser, D.; Woelper, C.; Schulz, S. *Chem.—Eur. J.* **2011**, *17*, 11394.

(8) Villinger, A.; Schulz, A. *Angew. Chem., Int. Ed.* **2010**, *49*, 8017.

(9) Schulz, S.; Lyhs, B.; Jansen, G.; Blaeser, D.; Woelper, C. *Chem. Commun.* **2011**, *47*, 3401.

(10) Schulz, A.; Villinger, A. *Chem.—Eur. J.* **2012**, *18*, 2902.

(11) Haiges, R.; Boatz, J. A.; Yousufuddin, M.; Christe, K. O. *Angew. Chem., Int. Ed.* **2007**, *46*, 2869.

(12) Haiges, R.; Schroer, T.; Yousufuddin, M.; Christe, K. O. *Z. Anorg. Allg. Chem.* **2005**, *631*, 2691.

(13) (a) *SMART V 5.625, Software for the CCD Detector System*; Bruker AXS: Madison, WI, 2001; (b) *SAINT V 6.22, Software for the CCD Detector System*; Bruker AXS: Madison, WI, 2001; (c) *SADABS, Software for the CCD Detector System*; Bruker AXS: Madison, WI, 2001; (d) Sheldrick, G. M. *SHELXS-90, Program for the Solution of Crystal Structure*; University of Göttingen: Göttingen, Germany, 1990; (e) Sheldrick, G. M. *SHELXL-97, Program for the Refinement of Crystal Structure*; University of Göttingen: Göttingen, Germany, 1997; (f) Sheldrick, G. M. *SHELXTL 6.12 for Windows NT/2000, Program*

library for Structure Solution and Molecular Graphics; Bruker AXS: Madison, WI, 2000.

(14) (a) *Bruker Instrument Service v2011.4.0.0*; Bruker AXS: Madison, WI, 2011; (b) *SAINT V7.68A*; Bruker AXS: Madison, WI, 2009; (c) *SADABS V2008/1*; Bruker AXS: Madison, WI, 2008; (d) *Bruker SHELXTL V2011.4-0*; Bruker AXS: Madison, WI, 2011; (e) Sheldrick, G. M. *Acta Crystallogr.* **2008**, *A64*, 112−122.

(15) Farrugia, L. J. *J. Appl. Crystallogr.* **1997**, *30*, 565.

(16) Zhao, Y.; Truhlar, D. G. *Theor. Chem. Acc.* **2008**, *120*, 215.

(17) Frisch, M. J.; Trucks, G. W.; Schlegel, H. B.; Scuseria, G. E.; Robb, M. A.; Cheeseman, J. R.; Scalmani, G.; Barone, V.; Mennucci, B.; Petersson, G. A.; Nakatsuji, H.; Caricato, M.; Li, X.; Hratchian, H. P.; Izmaylov, A. F.; Bloino, J.; Zheng, G.; Sonnenberg, J. L.; Hada, M.; Ehara, M.; Toyota, K.; Fukuda, R.; Hasegawa, J.; Ishida, M.; Nakajima, T.; Honda, Y.; Kitao, O.; Nakai, H.; Vreven, T.; Montgomery, J. J. A.; Peralta, J. E.; Ogliaro, F.; Bearpark, M.; Heyd, J. J.; Brothers, E.; Kudin, K. N.; Staroverov, V. N. K., R.; Normand, J.; Raghavachari, K.; Rendell, A.; Burant, J. C.; Iyengar, S. S.; Tomasi, J.; Cossi, M.; Rega, N.; Millam, N. J.; Klene, M.; Knox, J. E.; Cross, J. B.; Bakken, V.; Adamo, C.; Jaramillo, J.; Gomperts, R.; Stratmann, R. E.; Yazyev, O.; Austin, A. J.; Cammi, R.; Pomelli, C.; Ochterski, J. W.; Martin, R. L.; Morokuma, K.; Zakrzewski, V. G.; Voth, G. A.; Salvador, P.; Dannenberg, J. J.; Dapprich, S.; Daniels, A. D.; Farkas, Ö.; Foresman, J. B.; Ortiz, J. V.; Cioslowski, J.; Fox, D. J. *Gaussian 09*, Revision A.02; Gaussian, Inc.: Wallingford, CT, 2009.

(18) Goerigk, L.; Grimme, S. *Phys. Chem. Chem. Phys.* **2011**, *13*, 6670.

(19) Valero, R.; Gomes, J. R. B.; Truhlar, D. G.; Illas, F. *J. Chem. Phys.* **2008**, *129*, 124710/1.

(20) Zhao, Y.; Truhlar, D. G. *J. Chem. Theory Comput.* **2011**, *7*, 669.

(21) Dunning, T. H., Jr. *J. Chem. Phys.* **1989**, *90*, 1007.

(22) Peterson, K. A.; Yousaf, K. E. *J. Chem. Phys.* **2010**, *133*, 174116/1.